ORIGINAL PAPER

Experimental investigation of hybrid laminar flow control by a modular flat plate model in the DNW-NWB

Heinrich Lüdeke[1] · **Christian Breitenstein**[1,2]

Abstract

To determine the characteristics of new suction concepts for hybrid laminar flow control (HLFC) a modular flat plate wind tunnel model is investigated in the *DNW-NWB* wind tunnel facility. This approach allows detailed examination of suction characteristics in consideration of realistic boundary layer flow conditions. The following evaluation reveals the effects of joining methods between successive panels and other surface disturbances of porous materials and underlying chambers on HLFC techniques. After successful measurements with and without suction panels, this paper compares experimental results with theoretical and numerical approaches and draws conclusions from *N*-factor results and boundary layer (BL) measurements.

List of symbols

a	Suction tap distance [µm]
BL	Boundary layer
b_{Tape}	Tripping tape width [mm]
CF mode	Crossflow mode
CFD	Computational fluid dynamics
GFK	Glass fibre
c_p	Pressure coefficient
c_Q	Suction rate
d	Pore diameter [µm]
δ_1	Displacement thickness [mm]
E	Spectral energy [m²/s]
f_{Tr}	Transitional mode frequency [Hz]
H_{12}	Shape factor
HLFC	Hybrid laminar flow control
h_{tape}	Tape thickness [µm]
IR	Infra red
L	Model length [m]
LFM	Laminar flow meter
LST	Linear stability theory
n	n factor for each frequency
N	Envelope N factor
N_{crit}	Critical N factor
p	Surface porosity [%]
$\text{Re}_{h,\text{crit}}$	Critical step Reynolds number
Re_{Tr}	Transition Reynolds number
TS mode	Tollmien Schlichting mode
U_∞	Inflow velocity [m/s]
x	Streamwise position [mm]
x_{Tape}	Tape position [mm]
x_{Tr}	Transition position [mm]
z	Wall normal position [mm]
$DNW-NWB$	Windtunnel facility Braunschweig
RANS	Reynolds averaged Navier Stokes
NLF	Natural laminar flow
LFC	Laminar flow control

✉ Heinrich Lüdeke
heinrich.luedeke@dlr.de

Christian Breitenstein
c.breitenstein@tu-braunschweig.de

1 Deutsches Zentrum für Luft- und Raumfahrt, Institut für Aerodynamik und Strömungstechnik, Lilienthalplatz 7, 38108 Brunswick, Germany

2 Present Address: Technische Universität Braunschweig, Institut für Strömungsmechanik, Hermann-Blenk-Straße 37, 38108 Brunswick, Germany

1 Introduction

One current exploratory focus in aircraft wing design is the development of laminar flow technologies and appropriate suction surfaces for active flow control like LFC and HLFC.

To maximize the extent of laminar flow regions by delaying transition from laminar to turbulent, different approaches are utilized. The approach of NLF (natural laminar flow) optimizes the wing and airfoil profile geometry to generate a favorable pressure gradient (see [1]). Laminar flow control (LFC) is an active form of control to maintain laminar flow in the boundary layer over the entire wing profile. Finally, hybrid laminar flow control (HLFC) is a combination of LFC in the fore section of the wing profile, followed by an NLF geometry. Particularly, the general objective of these flow control techniques is a significant reduction of skin friction drag, which can represent up to 50% of the total drag of a typical civil transport aircraft by delaying the laminar-turbulent transition of the boundary layer. In the context of HLFC application, the *Institute of Aerodynamics and Flow Technology* at *DLR* conducts wind tunnel experiments and flight tests of suction based laminar flow control concepts on different technologically relevant model configurations [2, 3]. For this purpose surface parts of the particular model are provided with a microperforation that enables boundary layer control in the near-wall region by steady suction and thereby suppress transition at this position. A similar concept was also investigated on the vertical tailplane of an A320 aircraft in flight tests by Airbus (Fig. 1, [4]). On this A320 fin, the HLFC system was mainly used to control crossflow (CF) transition, generated by the unstable three dimensional boundary layer of the fin directly behind the nose, and instabilities from the similarly unstable attachment line boundary layer at the nose. Both transition mechanisms can be controlled by the HLFC approach, generating a stabilized BL.

However, especially under off-design conditions TS modes can be amplified downstream as well. For the present study, the focus is on TS-modes of the flat plate BL without cross flow parts to investigate properties of the porous surfaces. For simplification CF-modes are not considered in the following.

Now, for designing efficient suction systems, a determination of suction characteristics through the microperforated surfaces is required, as well as providing high surface quality for technical applications like the *A320* fin for free flight experiments. To examine such characteristics under controlled wind tunnel conditions a modular suction test rig was designed and manufactured using a modular flat plate configuration for the *DNW-NWB* test section (Deutsch Niederländische Windkanäle, Niedergeschwindigkeits Windkanal Braunschweig). This approach offers the possibility to examine suction characteristics of porous surfaces in consideration of realistic boundary layer flow (Fig. 2). The closed test section of the *DNW-NWB* enables laminar investigations at high *N*-factors, as demonstrated in former studies by Rohardt [2] and Bergmann [5]. While the first investigation determined the critical *N*-factor of ≈ 11.8 on a laminar airfoil by LST results, the second one determined the very low background noise level of the open and closed empty test section up to 40 kHz at an expected turbulence level of about 0.05%. The latter results explain the large *N*-factor for standard NWB models, which will be verified for the introduced test rig by spectral investigations of different BL profiles. *N*-factors in the above range were found in several other studies in the closed *DNW-NWB* test section concerning laminar flow control during the last decade.

Boundary layer suction is applied continuously along surface regions of the model through a laser drilled, microperforated suction sheet; more advanced materials will be investigated during future wind tunnel campaigns [6]. The model is equipped with two rows of pressure taps, particular transition positions are determined by utilizing three infrared cameras. A displaceable hot wire allows time resolved
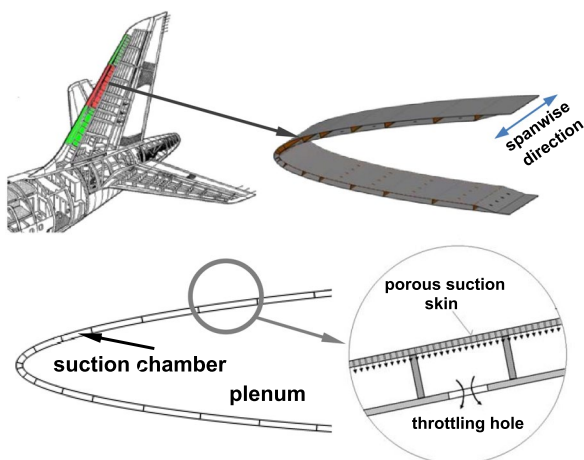

Fig. 1 Suction concept on an *A320* fin for flight experiments as an overview of the HLFC technique and the suction chamber concept [4]
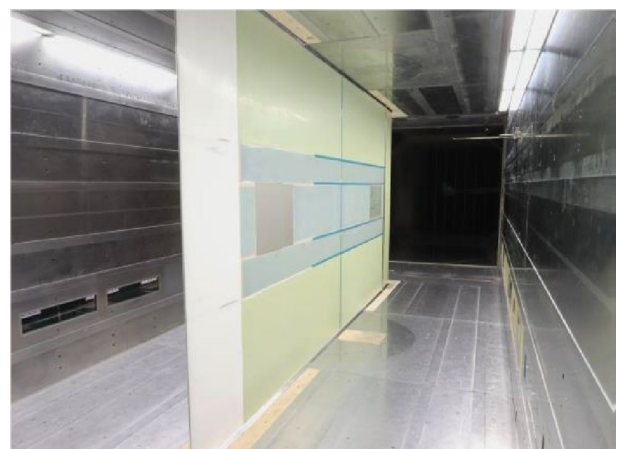

Fig. 2 Flat plate of 5 m length inside the closed test section of the *NWB*

measurement of boundary layer profiles including spectra of amplified Tollmien–Schlichting waves.

The modular design of the plate enables exchanging particular panels with different functionality and thereby modifying size and position of the suction region. A high-precision laminar flow meter (LFM) is used to measure the respective volume flow rate and thereby the suction rate. Inflow velocities between $20 \frac{m}{s}$ and $60 \frac{m}{s}$ lead to Reynolds numbers of 6.8×10^6 up to 20.6×10^6, the suction rate $c_Q = \frac{V_{\text{suction}}}{U_\infty}$ is varied between 0 and −0.001. Furthermore, adhesive tapes are placed on the model and alternatively on suction panels to investigate the effect of steps at different height and position [4].

The experimental results will be compared with CFD simulations of the model inside the closed wind tunnel test section, including the predicted transition position based on linear stability theory (LST). Comparisons of pressure distributions, boundary layer profiles and transition lines allow the validation of different calculation methods. Consequently, this study is an evaluation of wind tunnel results, as well as a comparison of the measurements with numerical data for validation.

For comparative RANS simulations the unstructured *DLR TAU-Code* is used [7]. Boundary layer and linear stability calculations are carried out by combining the numerical tools *Coco* [8] and *Lilo* [9]. Based on the transition position, extracted from infrared (IR) thermography, and the computed amplification factors of unstable modes, critical *N*-factors are determined and the characteristics of measured and computed Tollmien–Schlichting waves (TS waves) are compared. Finally, apart from the well-known primary effects of boundary layer suction on the significant instabilities, especially the influence of side effects becomes apparent. This may be of particular interest for manufacturing of laminar surfaces.

2 Experimental procedures

2.1 The DNW-NWB

The low speed *DNW-NWB* facility in Braunschweig is a subsonic wind tunnel, following the Göttingen design. The experiments discussed in the following are carried out in the closed test section with a cross section of 3.25 m × 2.8 m and a length of 8 m. A sketch of inlet and working section, including the flat plate model is shown in Fig. 3.

For investigations of laminar flow control by suction panels with different model setups, reliable high-quality laminar flow conditions are necessary. This is one central reason for the choice of this facility. Furthermore, the sufficiently
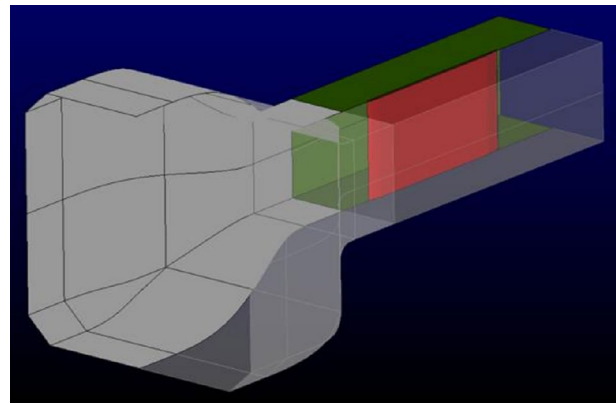

Fig. 3 Model of inlet and flat plate (red) installed in the closed test section of the *NWB*, as used for CFD simulations under assumption of a horizontal symmetry condition in the mid-section plane
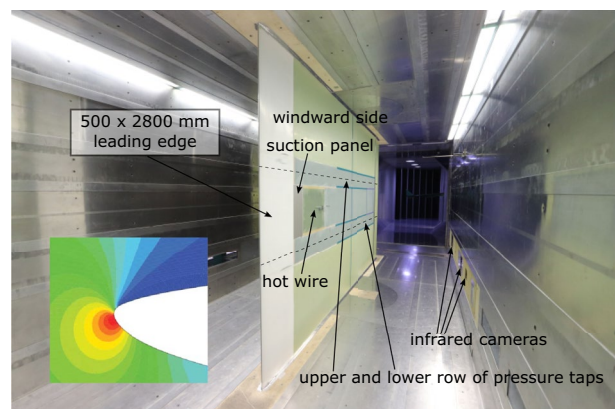

Fig. 4 Instrumentation of the flat plate installed in the closed test section of the *DNW-NWB*. Inset: pressure contours in the region of the superelliptic asymmetrical nose

large test section allows various setups with different suction panels or additional instrumentation.

2.2 Model setup

Figure 4 illustrates the setup of the model with a total length of $L = 5$ m and an exemplary arrangement of the middle panel row, which has a width of 500 mm. As an overview, some of the applied measurement systems are shown. Since all panels in this region are freely interchangeable, arbitrary arrangements of the middle part are possible. Suction panels of 0.2 m (see Fig. 4) and 0.4 m length were manufactured. For structural reasons chambers composed from brass profiles are placed under the microperforated surface which is connected with a plenum underneath by throttling holes (Fig. 5).
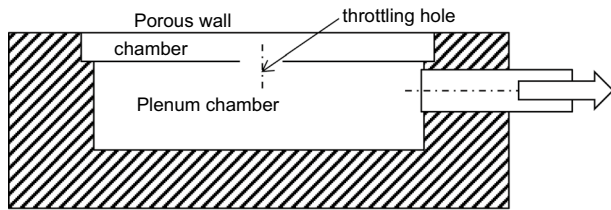
Fig. 5 Composition of suction panels with chambers and plenum

Fig. 6 Infrared image of the transition line at an inflow velocity of $40\,\frac{m}{s}$ for the case with no installed suction panel

To equalize the chamber pressure, all chambers are connected by additional drilling holes for both suction panels. The technique of separately sealed suction chambers (see Fig. 1) was already validated on more complex fin geometries investigated in other wind tunnels to keep adjustment of the outer pressure distribution in each porous wall section. The principle of this type of suction panels is illustrated in Fig. 5. All suction surfaces are provided with laser drilled pores at a diameter of $d = 50\,\mu m$ and a distance of $a = 500\,\mu m$ yielding a porosity of $p = 0.79\,\%$. Suction and volume flow control can be combined by the use of a high-precision laminar flow meter (LFM). The investigated porous material was tested with respect to uniform suction by the LFM during preceding validations for experiments on other HLFC models with the same suction sheet, including successful measurements of uniform material porosity. In addition, single chamber pressures for the panels were determined during all tests without finding pressure gradients in streamwise direction within the measurement tolerances.

Geometric tolerances are prescribed for manufacturing by an allowed wavyness of 0.4 mm for 50 mm suction chamber width and sandpaper roughness for all suction and GFK panels below 6 micron. Steps between adjacent panels are chosen below 40 micron using Plasticine along panel gaps. Finally, relevant suction non uniformities would have been determined by IR visualizations of transition lines.

To correct a spurious additional angle of attack resulting from manufacturing and installation tolerances, the whole model of the plate is vertically mounted between two rotatable discs at its center axis. By this way, a relative correction angle of 0.15 ° is preset, which is kept small, due to the size of the model and the resulting forces. To match the required pressure distribution from CFD, a trailing edge angle of 2.8 ° is chosen using the freely adjustable trailing edge of the model. As well as the asymmetric geometry of the nose, those parameters follow from prior design optimization regarding the predicted transition position. Thus, it is secured that the boundary layer along the panels approximates a Blasius boundary layer at low pressure gradient on the one hand and on the other hand transition occurs downstream of the nose on the interchangeable panels under all considered flow conditions.
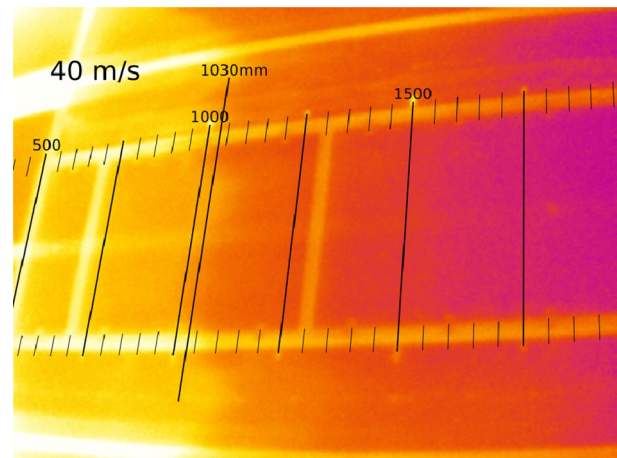
To determine the overall suction rate c_Q the wall normal volume flow rate needs to be measured at high precision during the wind tunnel tests. Suction characteristics of the described porous surfaces were identified during preliminary studies by means of the DLR laminar flow meter (LFM), designed by Seitz [10] for this specific purpose. The LFM is manufactured from a highly accurate set of tubes at given length, determining the laminar pipe flow by the pressure drop along these tubes. Special care is taken on in- and outflow end effects of the pipe flow, using an iterative procedure to increase accuracy of the resulting mass flow significantly. For the experiments discussed in this paper, the LFM is also used to determine the volume flow rate through the porous surface, which is consequently adjusted with the same precision as in the calibration run for suction characteristics before. The plate is equipped with two symmetric rows of 62 pressure taps each (upper and lower row in Fig. 4). Microelectromechanical pressure sensors allow for measurements at a high precision of 7 Pa. Outside of the wind tunnel test section, three infrared cameras of different resolutions are arranged to observe the flat plate from three perspectives and thereby allow for a determination of the transition position on the windward side of the plate (Fig. 6).

To improve the contrast in the infrared image, the temperature difference between surface and boundary layer can be increased. For this purpose, parts of the plate can be heated by means of carbon fibre fabric (Fig. 7). The particular mats are connected in series to maximize the total electric resistance, so high thermal power can be achieved at relatively low amperage. During the measurements, temperature is continuously monitored by using PT100 temperature sensors.
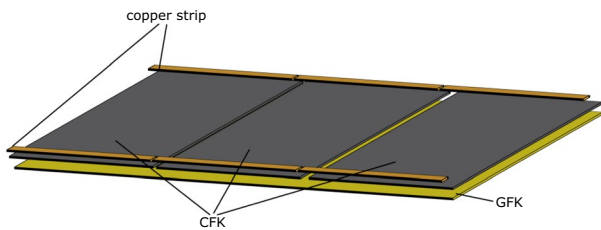
Fig. 7 Heatable carbon fibre fabric inside a panel of 600 *mm* length, separately electrically connectable
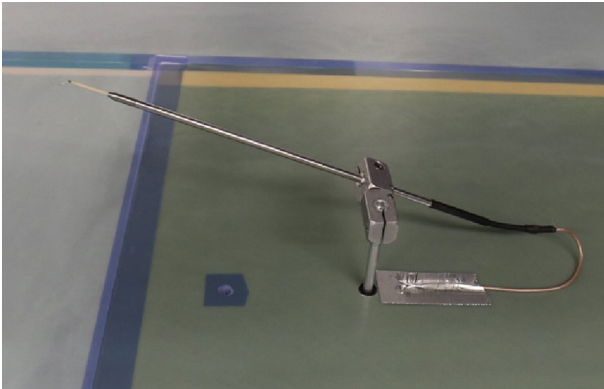

Fig. 8 Displaceable hot wire anemometer with probe holder and probe on a separate GFK panel

2.3 Hot wire anemometry

By means of a displaceable hot wire anemometer the velocity profiles inside the boundary layer at the positions $\frac{x}{L} = 0.202$ (1010 mm) and $\frac{x}{L} = 0.740$ (3700 mm) are measured. Fig. 8 shows the installed probe with holder, the respective traverse is located inside of the model behind the GFK surface. This GFK panel with probe holder is mounted at two different positions for the measurements. At the forward position $\frac{x}{L} = 0.202$ (1010 mm) the hot wire is moved between $z = 0.5$ mm and $z = 20$ mm along the surface normal. Because the boundary layer at $\frac{x}{L} = 0.740$ (3700 mm) is turbulent and thereby thicker, the required hot wire range is chosen between $z = 1$ mm and $z = 40$ mm here. The investigated instabilities require a frequency resolution of 10000 Hz. Hence, the measurements provide averaged and statistical quantities of the boundary layer, but furthermore spectral data as well.

In comparison with requirements for turbulent spectra, a relatively low frequency margin is provided, which is still adequate for TS wave resolution, as demonstrated by LST studies later on. The hot wire post processing is carried out using a Hanning filter at a measurement time of 14 s for each wall normal point. Using these parameters, the lowest resolved frequency in the spectra after post processing

is prescribed at 30 Hz, while the largest is 5000 Hz under consideration of the Nyquist sampling theorem. A standard procedure of subdividing the temporal sample into a number of sub intervals and averaging the resulting spectra is used by the hot wire analysis software.

2.4 Measuring program

The first test series for velocities between 20 $\frac{m}{s}$ and 60 $\frac{m}{s}$ are reference measurements without artificial steps and without suction. Subsequently, adhesive tapes of heights between 60 µm and 80 µm are placed at different positions in the nose region to examine step effects. Such cuts from welded suction surfaces are expected for realistic flight cases and the effect on transition has to be investigated for different porous materials. Additional influences resulting from steps on the suction panel were investigated by Breitenstein in [11]. Hot wire measurements are carried out directly behind the 200 mm suction panel at different suction rates.

3 Numerical procedures

3.1 CFD simulation

CFD simulations, providing surface pressure distributions on the plate were performed with the unstructured DLR TAU-code [7] within preliminary studies regarding the model design. Assuming symmetrical flow using a horizontal symmetry plane, three-dimensional RANS simulations of an idealized model geometry installed in the closed test section behind the nozzle are carried out (Fig. 3). Three inflow velocities of 20 $\frac{m}{s}$, 40 $\frac{m}{s}$ and 60 $\frac{m}{s}$ are considered; combined with the plate length $L = 5$ m one obtains Reynolds numbers between 6.8×10^6 and 20.6×10^6. The blunt superelliptic nose was designed by using these simulations, providing a transition line behind the end of the curved nose part, where flat interchangeable panels are mounted on the models plane part. To keep the transition line in this area, where the suction surfaces can be placed, a high aspect ratio for the windward superelliptic nose part was necessary and consequently a thin windward half of the nose profile (see Fig. 4: inset). At a given model thickness of 100 mm for instrumentation, the other side of the nose had to be a thick superelliptic shape, which was slightly modified to guarantee the transition requirements.

The turbulent boundary layer in the region downstream of the surface is modeled by means of a one equation Spalart–Allmaras model to correctly reproduce the physical behaviour of an attached boundary layer. Amongst others, this avoids unsteady, laminar trailing edge separation, what would result in spurious pressure distributions along the whole surface. Starting from the leading edge

up to a preliminary fixed transition at $\frac{x}{L} = 0.16$ a laminar boundary layer is simulated; downstream of this position, turbulent boundary layer conditions are expected. This $\frac{x}{L}$ was taken from linear stability theory at the maximum Reynolds number and a prescribed critical N-factor from former studies [12]. For this transition treatment, carried out by simply starting the turbulence model behind a given coordinate, influences on the wall pressure distribution are neglectable, as shown by different additional CFD simulations. The turbulent BL is also compared with hot wire measurements. The pressure distribution is used for BL-computation, based on similarity theory as well as for validation of the pressure measurements at the model surface.

3.2 Boundary layer calculation and transition prediction

A widely used tool for transition prediction is the e^N-method, that is derived from linear stability theory (LST). Here, local amplification rates of dominant Tollmien–Schlichting instabilities (TS modes) at different frequencies are calculated from two-dimensional BL velocity profiles. For each unstable mode, those amplification rates are integrated to an amplitude ratio with respect to an initial amplitude. The logarithm of this amplitude ratio is called n-factor of the respective frequency and describes a curve along the streamwise coordinate. Transition is assumed where the envelope, which is the maximum of the n-factors of all considered frequencies, exceeds a specific, critical amplitude ratio. This envelope is called N-factor; the critical amplitude ratio is called N_{crit} and represents an empirical element of the method, that needs to be determined by comparison with wind tunnel results. N_{crit} usually depends on the incoming turbulence intensity and spectrum as well as on the geometric model characteristics and wind tunnel blockage. Thus, transition positions from infrared measurements will be compared with linear stability theory in the following. Velocity profiles required for the e^N-method can be extracted directly from highly accurate CFD simulations or calculated from similarity theory and pressure distributions from these simulations. The latter provides second derivatives of much higher quality in the near wall region, which is of major importance for transition prediction quality. Hence, this approach is used in the following. On the basis of pressure distributions from CFD and a given suction rate along porous wall segments, the BL solver COCO [8] computes velocity profiles for LST calculations by the appropriate tool LILO [9], calculating finally N-factor curves for comparison with IR data. In the following, the displacement thickness δ_1 is taken from COCO for all laminar profiles.

3.3 Tollmien–Schlichting waves in the flat plate boundary layer

A discretisation of the pressure distribution in streamwise direction for computing particular velocity profiles between leading edge and $\frac{x}{L} = 0.4$ (2000 mm) contains 1200 stations, interpolated from CFD surface pressure data. The stability solver starts its search for unstable modes at a given station, tracing in both directions, upstream and downstream. In the following, the center of the suction area at $\frac{x}{L} = 0.12$ (600 mm) is chosen as a starting point to ensure, that unstable regions are considered in front and behind the suction panel. The estimated frequency range of amplified modes is divided into 100 discrete frequencies and resulting amplification rates are integrated to n-factors along the streamwise wall coordinate. As already mentioned, the obtained N-factor envelope in combination with transition positions from experiments allows determining N_{crit} at the chosen flow conditions.

4 Results

4.1 Surface pressure distribution along the model

Figure 9 shows the pressure distribution in streamwise direction for $U_\infty = 60 \frac{m}{s}$ along two spanwise positions, an upper and a lower cut. The plate is mounted vertically, so the upper and lower row of pressure taps on the windward side are visible in Fig. 4. This diagram compares the measured pressure distribution without suction wall with the pressure distribution from CFD data.
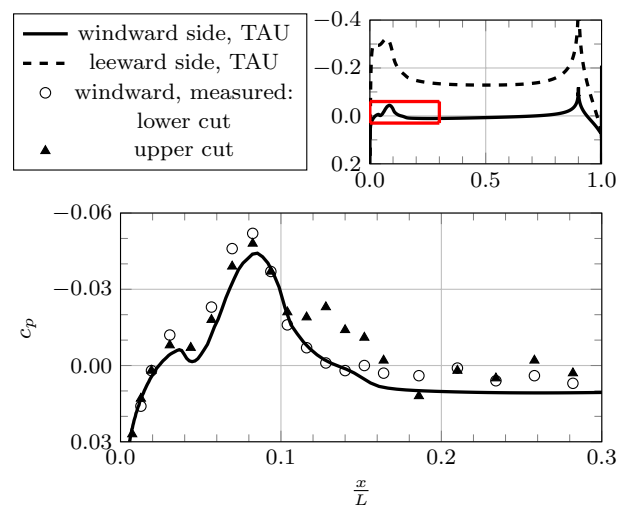

Fig. 9 Measured pressure distributions at two spanwise positions compared to CFD simulations for $U_\infty = 60 \frac{m}{s}$

As mentioned above, the pressure distribution was designed with the aim of positioning transition for the widest possible range of Reynolds numbers in the flat plate region behind the nose, where IR thermography of transition lines is possible and interchangeable suction panels can be placed. These requirements and the smooth geometric transfer from nose to plate result in a superelliptic, asymmetrical nose geometry that is shown in the inset of Fig. 4. In [13] Methel et al. applied an alternative design goal, to reduce the suction peak, and also obtained an asymmetric nose geometry. The design of a symmetric nose was demonstrated by Grappadelli et al. in [14], which is not appropriate for these experiments at the given model thickness, due to the required half-axis ratio of the windward nose part. The obvious difference between those geometries and the present nose geometry is the double suction peak shown in the pressure distribution in Fig. 9. This is a result from the design process with the goal of prescribed transition positions, based on linear stability analysis.

As already demonstrated in [11], the inflow velocity and thus the Reynolds number shows low significance for the pressure distribution of this geometry. A comparison between measured and calculated pressure distributions shows better agreement with simulations in the lower section, while significant deviations appear in the other cut. A major reason for these differences is the associated instrumented panel, which requires a step-free connection to the center section for avoidance of premature transition. To achieve this important goal, a slight deformation of the respective panel had to be accepted and consequently a deviation in the associated row of pressure taps is visible. These preliminary investigations have shown that even slight deformations of individual panels can lead to significant deviations of the measured pressure distribution from the simulations with nominal geometry, but that such deviations generally have a minor influence on the transition position.

It should also be noted, that the largest pressure gradient behind the minimum roughly coincides with the region, where suction was applied. Therefore, most evaluations are carried out with the 200 mm suction panel, placed directly behind the nose at $\frac{x}{L} = 0.1$. The effect of this setup on transition, including BL suction will be discussed below.

4.2 Boundary layer profiles

BL velocity profiles were determined in wall normal direction by hot-wire measurements at two positions with and without suction. Figure 10 shows the profiles at $\frac{x}{L} = 0.202$ (1010 mm). The turbulent results from TAU and the laminar results from the boundary layer solver COCO are plotted in comparison with hot-wire results. As mentioned, TAU assumes turbulent flow downstream of fixed transition at $\frac{x}{L} = 0.16$, while the boundary layer solver depicts laminar
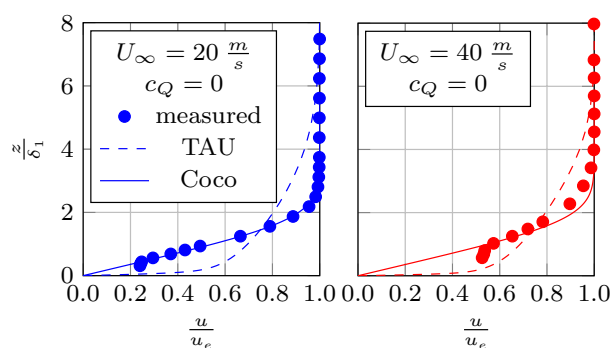
Fig. 10 Laminar boundary layer profiles at $x = 1010$ mm from hot-wire measurements, CFD simulations and boundary layer computations
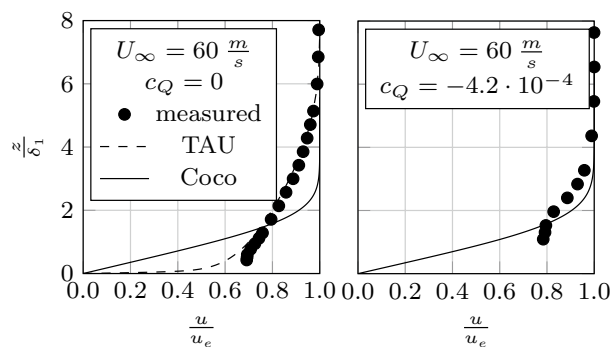
Fig. 11 Boundary layer profiles with and without suction at $x = 1010$ mm from hot-wire measurements, CFD simulations and boundary layer computations

results. Accordingly, the respective simulated velocity profiles differ significantly.

The shape factor from turbulent boundary layer simulations shows the expected value of $H_{12} = 1.4$, whereas the laminar velocity profiles result in good proximity in the standard value for laminar conditions of $H_{12} = 2.6$. By comparing the corresponding velocity profiles and shape factors from hot-wire output, the BL profile there is obviously laminar for an inflow velocity of 20 $\frac{m}{s}$ and turbulent for 60 $\frac{m}{s}$. At 40 $\frac{m}{s}$, neither laminar nor turbulent conditions can be observed for the boundary layer, and neither a clearly laminar nor a fully turbulent profile appears.

Comparison with energy spectra from hot-wire measurements [11] confirms the assumption, that this profile is in a transitional state, which is also true for the case at 60 $\frac{m}{s}$ including suction at $c_Q = 4.2 \times 10^{-4}$ (see Fig. 11). This is in contrast to the fully turbulent profile at 60 $\frac{m}{s}$ without suction. Since the suction panel is located upstream of the hot-wire position, no direct suction influence on the BL profile is possible, but the boundary layer is essentially influenced by the transition displacement and the smaller BL thickness.
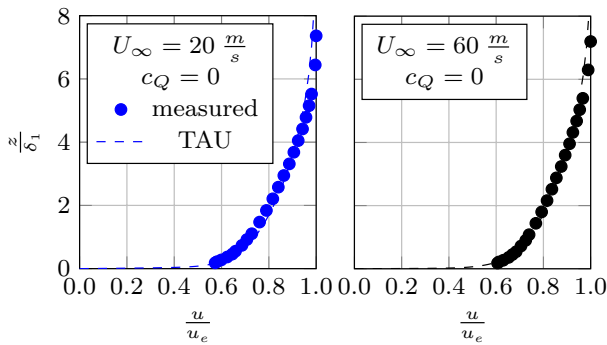
Fig. 12 Turbulent boundary layer profiles at $x = 3700$ mm from hot-wire measurements and CFD simulations

Accordingly, the laminar boundary layers determined by the BL solver are approximately self similar with respect to the local displacement thickness δ_1 for all cases with and without suction.

In the near wall region, hot-wire data from this position indicates stronger curvature of the velocity profile towards higher velocities. A possible explanation for this deviation may be slight vibrations of the hot-wire probe, causing that the actual distance from the wall indicates larger values than specified by the traverse.

Figure 12 compares velocity profiles at $\frac{x}{L} = 0.740$ (3700 *mm*), which show turbulent behavior at all conditions, so only CFD-RANS results will be compared with hot-wire data. At this position, all profiles match RANS simulations in good agreement. The first near wall data point for this case is twice as distant due to the thicker turbulent boundary layer and therefore less critical with respect to spurious near wall velocity magnitudes.

4.3 Effects on the transition position

4.3.1 Evaluation of infrared images

For each measuring point, the transition location is determined from an associated infrared image. Two possibilities are available for the evaluation. On the one hand, infrared images can be evaluated manually, and the transition line will be subject of subjective impressions of the observer, on the other hand, an automatic transition evaluation is possible. In this case, transition lines are determined by software tools, specially developed within former HLFC tests. These tools use individual pixel brightness as an objective criterion for distinguishing between laminar and turbulent regions; a more detailed description can be found in [15]. The comparison of both methods by Breitenstein [11] shows negligible differences of both evaluations at selected inflow conditions. Therefore, manually determined transition positions will be used for the following discussion.

4.3.2 Step influences

For transport aircraft configurations, steps between individual elements of the wing are unavoidable. They occur, for example, at the high-lift system or at intersections between surface elements when suction sheets are used for flow control. Especially, the effect of steps on the transition position, generated by suction surface intersections must be taken into account for laminar flow control on wings with suction or for the laminar wing design [16, 17]. Consequently, the influence of tapes on the transition will be discussed for closed walls in the following and for suction panels in Sect. 4.4.

Figure 13 shows transition shifting due to an influence of different steps with a closed wall. As shown in the inset, an adhesive 18 mm wide strip (blue line at the inset of Fig. 13) was used to introduce a forward and a backward facing step in the near wall boundary layer. This adhesive strip only extends in the lower half of the considered area. This technique visualizes transition shifts as a direct result of the additional disturbances caused by the steps, since the other part is identical with IR data from experiments without step. The stated tape position for all following cases corresponds with the tapes trailing edge, i.e. with the recessed step, since this coordinate is more critical for transition displacements. Furthermore, for all investigated steps a tape width of $b_{tape} = 18$ mm is chosen.

At 20 $\frac{m}{s}$ inflow velocity, transition will appear far downstream due to the low Reynolds number and the increased boundary layer thickness, consequently all arising steps will have no visible influence on the transition under
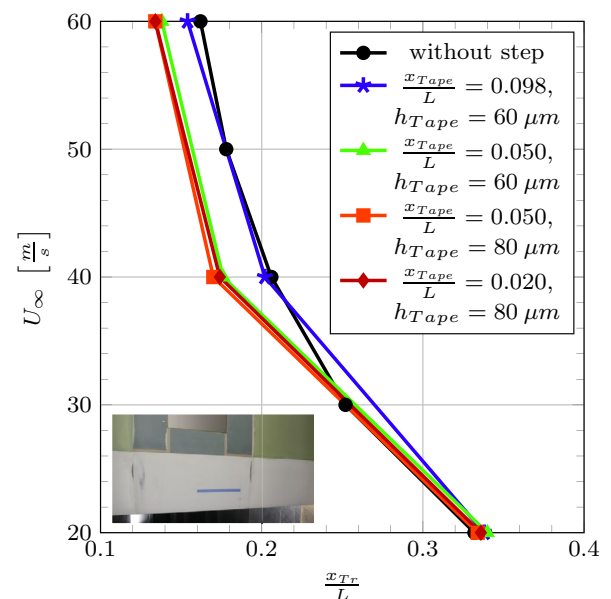

Fig. 13 Effect of steps on the transition position for tapes of different height at varying positions. The blue line in the inset is the tape at one position on the model nose

these conditions. For $60 \frac{m}{s}$ at a tape position of $\frac{x}{L} = 0.02$ (100 mm), and a maximum tape thickness $h_{tape} = 80\mu m$, the ratio between tape height and local displacement thickness reaches its maximum value of about 0.3. The step Reynolds number $Re_h = h \times U_\infty / \nu$ with ν as the kinematic viscosity under wind tunnel conditions, reaches its maximum of $Re_h \approx 330$ as well. It is thus well below the critical value of $Re_{h,crit} = 900$, empirically given by Nenni and Gluyas [18]. However, Schrauf points out in [16] the widely studied fact that such a criterion based solely on Re_h is not applicable near the neutral point of the relevant modes, since the boundary layer is particularly sensitive to surface perturbations at this position.

Recent detailed numerical investigations have shown, that the empirical criterion of Nenni and Gluyas [18] is not applicable for all cases of forward or backward steps. It can be stated consequently, at larger inflow velocities, transition is strongly influenced by surface perturbations if they are located immediately upstream of the neutral point. This neutral point belongs to the critical Tollmien–Schlichting wave from transition without steps, demonstrated in Fig. 14. Thus, comparison of transition positions in Fig. 13 and the corresponding LST diagrams in Fig. 14 shows under the investigated conditions, not the step height is dominant for transition shifts but mostly the tape position is decisive. For this reason, the tape position at the nose was chosen by neutral point of the most critical n-factor curve, where surface perturbation influences are most important. In the scope of Fig. 14, the procedure to determine N_{crit} can be described as well. Form the wall pressure distribution BL-profiles and n-factor curves are generated, so the resulting envelope allows at a given transition position from IR data the extraction of N_{crit} at the investigated conditions.
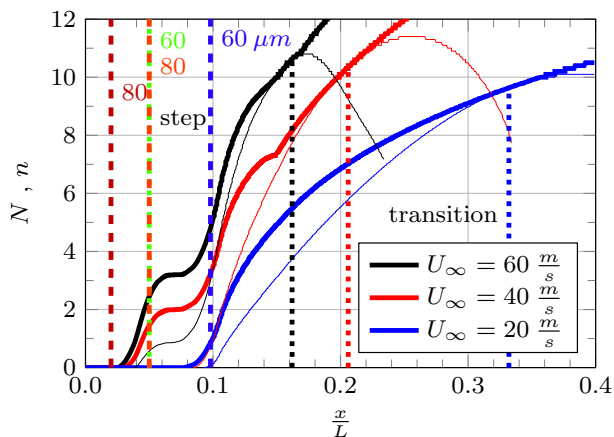
4.3.3 Boundary layer suction

In the next step, suction influences on the BL transition process are investigated. For this purpose, a constant suction velocity is specified in the area of a 200 mm panel between $\frac{x}{L} = 0.1$ and $\frac{x}{L} = 0.14$ in the BL solver COCO to generate velocity profiles for LST by the separate tool LILO. This is a standard procedure for suction surfaces at given pressure distribution, successfully applied in former wind tunnel studies [4]. All these studies expect the pressure to be unaffected by the suction at realistic but small c_Q. The transition Reynolds number is determined from infrared data. Figure 15 compares influences of boundary layer suction on the transition Reynolds number from measurement and calculation. An assumed transition location was determined from N-factor curves of LST output by specifying a critical N-factor. The N_{crit} value is determined by calculating the N-factor curves from LST, using the transition position from IR visualizations to extract the critical value from the envelope (see Fig. 14 and Fig. 18). For better accuracy, N_{crit} was calculated for both inflow velocities by minimizing the sum of the deviation squares at the measured transition coordinates. The resulting transition Reynolds numbers agree in good approximation with the NWB infrared results.

Obviously, the curves from both inflow velocities in Fig. 15 differ significantly, despite the normalization to Re_{Tr}. The suction influence on the transition Reynolds number at $60 \frac{m}{s}$ is much stronger, since the suction changes the shape factor of the boundary layer, which in turn leads to the stronger shift in the normalized transition positions (see also [11, 19]).

A closer look at Fig. 15 shows, that transition initially moves approximately linearly downstream up to about $c_Q = -0.00025$. By a further increase of the suction rate above this value, transition moves only gradually further downstream. A similar behavior was observed by
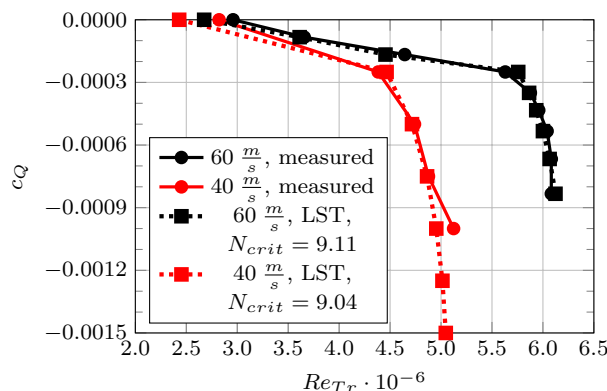

Fig. 14 N-factor curves (thick) and n-factor curves of the critical modes (thin) from LST and transition positions determined from infrared images

Fig. 15 Effect of suction rate on the transition reynolds number from infrared images and from LST

Grappadelli et al. in [14] at a similar suction rate. Comparison with corresponding shape factors shows that this limit at $c_Q = -0.00025$ is not characterized by reaching an asymptotic suction profile, which will appear at significantly higher suction rates. Instead, comparing transition positions from Fig. 15 with N-factor curves from LST in Fig. 16 demonstrates the reason for this behavior. Amplified modes are already found in the nose region, especially at pressure rise. In the suction region, these modes are damped again when the suction rate c_Q is sufficiently high. Complete damping is apparent above $c_Q = -0.00025$. A further increase of c_Q has consequently no direct influence on the N-factor growth behind the suction panel. It should be noted that LST results upstream of the panel are identical for all chosen conditions, since they are based on the same pressure distributions. For practical reasons, only N-factor curves for $c_Q < -0.00025$ are included upstream of the suction wall.

The fact that a slight additional transition shift can still be observed, even for larger suction rates c_Q (Fig. 15) results from the reduced displacement thickness of the extracted boundary layer, which decreases almost linearly with c_Q (see also [19]).

In a thinner boundary layer, the low frequency modes, which would lead to transition, are less amplified. Instead, higher frequency modes are growing and finally dominate
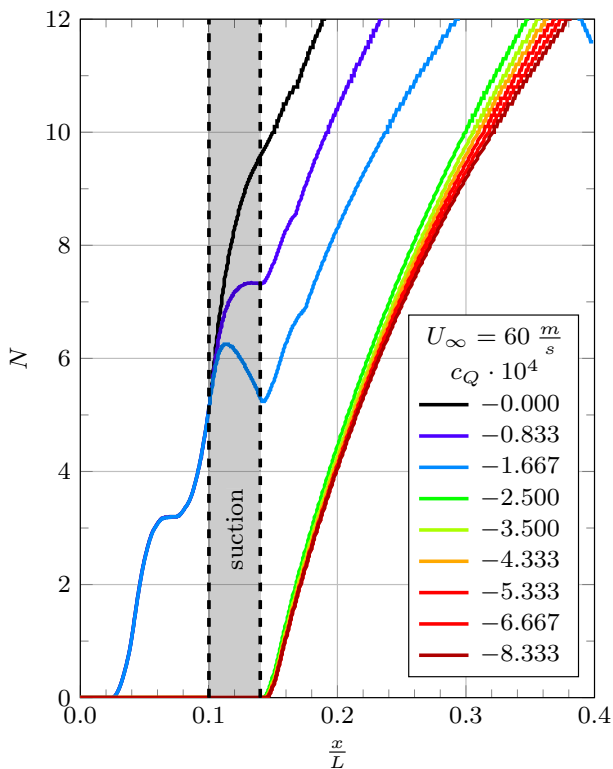
the transition process for large c_Q, as visible in Fig. 17. The frequency curve of critical modes leading to transition downstream (f_{Tr}) is plotted against the suction rate , as well, as the respective curves for the displacement thickness from the BL solver COCO. For low c_Q, an increase of the suction rate decreases f_{Tr} since transition is shifted downstream into a region where modes of lower frequency are strongly amplified. Stronger suction causes another f_{Tr} growth, since the transition position is kept nearly constant and the influence of a thinning boundary layer gains significance.

4.4 Determination of critical N-factors

In Fig. 18, three inflow velocities are chosen to demonstrate how the critical N-factor N_{crit} is determined from comparisons between transition lines without suction panel from IR
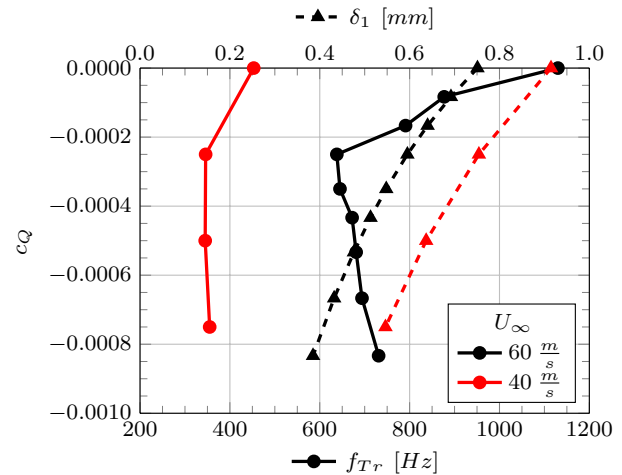

Fig. 17 Frequency of critical modes and displacement thickness from BL solver at the suction panels rear edge as a function of suction rate
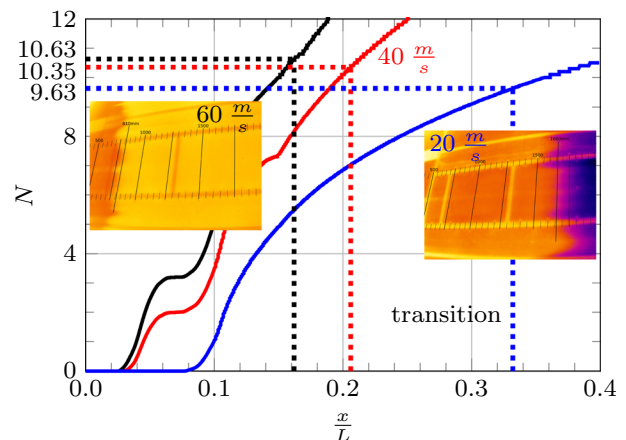

Fig. 16 N-factor curves for the plate with suction panel at different suction rates

Fig. 18 Effect of inflow velocity on the critical N-factor without suction panel

images and the corresponding N-factor curve from LST. For the inflow velocities $60\frac{m}{s}$ and $40\frac{m}{s}$, an N_{crit} of about 10.5 is obtained. Usually, a value of 11.8 is found for the closed test section [12], which was determined however for a laminar airfoil profile with a comparatively small wing chord and is therefore comparable with the present measurements to a limited extent only. Nevertheless, a value of 10.5 is still within the expected range.

For $20\frac{m}{s}$, the N_{crit} value decreases. This behavior can be explained by the flattening N-factor curve in the transition region, which is influencing the critical N-factor as well, since linear assumptions are generally violated near the transition line and corrected only by the empirical N_{crit} specification. The result of this broadened transition region is a slower transition to turbulence and a modification in N_{crit}. This broadened transition range is also evident from the infrared image at $20\frac{m}{s}$ (see IR images in Fig. 18).

Figure 19 shows the influence of BL suction on N_{crit} using the e^N method. In addition, the constant N_{crit} used in Fig. 15 to determine transition is plotted under both inflow conditions. In this figure, the data is shown for a 200 mm suction surface behind the nose, while in Fig. 18 the wall is completely closed. This difference alone results in an N_{crit} reduction at $60\frac{m}{s}$ even without active suction.

N_{crit} initially decreases for both inflow conditions at active suction. After increasing c_Q it fluctuates slightly around a value, well below the critical N-factor of the closed surface. This behavior is well known from previous laminar flow control experiments with the A320 fin model , but some explanations will be discussed in detail below [11].

In addition to the repeatedly mentioned influences of geometric surface perturbation, already excluded by several comparative measurements by the described application of additional steps from tapes, the suction surface roughness is generally a possible source of such effects. Under the present conditions, these factors can be largely excluded by estimating the roughness height [11]. Since the pressure
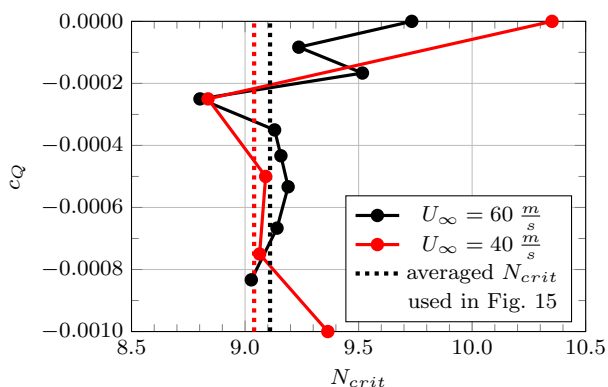
distribution along the suction panel still exhibits remaining small pressure gradients due to the nose design, the pressure difference along the porous surface in streamwise direction may generate a slight blowout or suction. While even small suction has a generally stabilizing on the boundary layer, blowing results in a much larger but destabilizing effect. This is another possible explanation for the reduced N_{crit}, but still needs numerical confirmations under NWB conditions.

In [20], Tilton and Cortelezzi present numerical studies suggesting influences of Tollmien–Schlichting waves over a porous wall on interacting instabilities in the plenum below. The resulting streamline diagram of this perturbation flow is shown in Fig. 20. Obviously, the unstable modes in the plenum interact with the TS waves on top. In their study, Tilton and Cortelezzi describe additional amplifications from these interactions and thus a destabilization of the unstable boundary layer. The fact that this phenomenon depends not only on porous wall properties, but also on the Reynolds number and the considered frequencies as well, provides a plausible explanation for the different N_{crit} decrease at different inflow conditions, when using suction panels in comparison with an entirely closed wall. Nevertheless, without detailed numerical studies of the interaction using the NWB flow conditions at the porous wall panel, this is still a hypothesis to explain the reduced N_{crit}.

Results from former experiments suggested an interaction between TS waves and the plenum flow below the porous wall with a resulting influence on the process of transition as well. In [13], Methel et al. describe how the transition on a flat plate is shifted upstream as the porosity of the surface increases. To rule out the possibility of additional porous wall roughness, causing this effect, Methel et al. sealed the suction surface on the lower side by adhesive tape. In this way the transition was shifted downstream, almost to the position where it was located without the porous wall [13]. This is the same tendency, found in the present experiments.

4.5 Spectral characteristics of critical modes

Hot-wire measurements at a maximum frequency of 10 kHz allow, in addition to the averaged BL velocity profile, an investigation of the velocity fluctuation as well as the associated
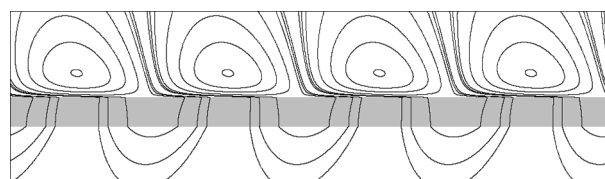

Fig. 19 Critical N-factor as a function of suction rate for different inflow velocities

Fig. 20 Interaction between TS modes in the boundary layer and modes inside the plenum (from Tilton and Cortelezzi [20])
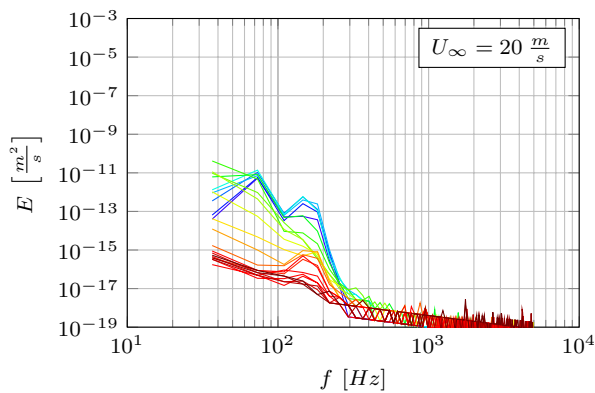
Fig. 21 Measured energy spectra at $x = 1010$ mm and at different wall distances z; laminar boundary layer for $U_\infty = 20\, \frac{\mathrm{m}}{\mathrm{s}}$

energy spectra for the measured wall-normal positions in the boundary layer.

Since spectral contents of TS waves in the laminar BL are of special interest, this relatively low frequency range was chosen, in contrast to investigations of purely turbulent velocity profiles. Figure 21 shows the BL energy spectrum at $\frac{x}{L} = 0.202$ (1010 mm) and 20 $\frac{\mathrm{m}}{\mathrm{s}}$ for all wall-normal positions of the probe except the data from near wall positions in Figs. 10 and 11. Transition occurs at $\frac{x}{L} = 0.332$, well downstream of the hot-wire position. The corresponding shape factor $H_{12} = 2.53$ confirms, that this energy spectrum is a result from a laminar boundary layer. The amplitudes exhibit a peak in the range between 70 Hz and 200 Hz, corresponding with the amplified Tollmien–Schlichting waves from LST simulations. According to this, the predicted frequency of the critical mode, leading finally to transition is found at $f_{\mathrm{Tr}} = 138\, Hz$.

The upper diagram in Fig. 22 shows the energy spectrum at 60 $\frac{\mathrm{m}}{\mathrm{s}}$, again at $\frac{x}{L} = 0.202$ without suction. The infrared images predict transition at $\frac{x}{L} = 0.162$, upstream of the hot-wire probe. The corresponding spectrum belongs to a turbulent boundary layer and shows residues of the critical TS modes at 400 Hz.

In the case of active suction at $c_Q = -4.167 \times 10^{-4}$ (Fig. 22 bottom), the transition location is determined at $\frac{x}{L} = 0.29$ and thus slightly downstream of the probe, while the calculated shape factor of $H_{12} = 1.826$ indicates a rather transitional boundary layer, which is also evident in the associated BL profile (Fig. 11).

The observed peak in the energy spectrum at about 500 Hz is thus somewhat lower than the frequency of $f_{\mathrm{Tr}} = 672\, Hz$ from LST predictions.

5 Summary and outlook

Basic investigations of boundary layer transition delay from wall suction were carried out within the presented experimental data analysis, including step influences on the
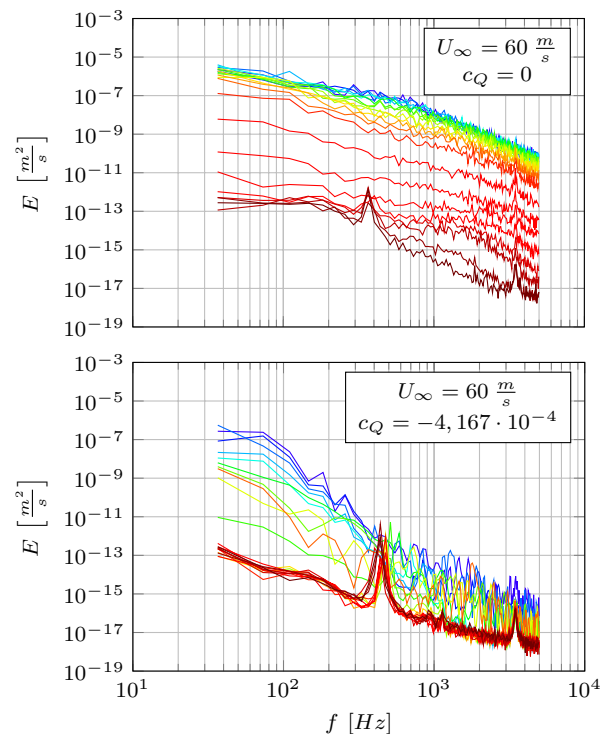

Fig. 22 Measured energy spectra at $x = 1010$ mm and at different wall distances z in a boundary layer with $U_\infty = 60\, \frac{\mathrm{m}}{\mathrm{s}}$ with and without suction

transition process and different suction coefficients for an interchangeable suction panel. For this purpose, data from pressure, hot-wire and infrared measurements, including energy spectra, were evaluated in comparison with numerical results from CFD as well as LST or e^N approaches respectively.

Pressure gradients along a flat plate geometry are generally assumed to be small, except in the nose region. For this configuration, the nose geometry is designed to keep approximately a blasius boundary layer, and at the same time transition has to occur behind the nose on exchangeable instrumented flat plate GFK panels. It is well known, that even slight deviations from the generic geometry may influence the pressure distribution and the transition line. In this context, the impact of steps on the BL stability is investigated by applying tapes of different thickness. It was found for the selected wall normal tape dimensions, that the corresponding step height is less decisive than the position and particularly the distance from the respective neutral point of the relevant Tollmien Schlichting wave.

Experiments with suction panels have been carried out to observe influences of BL suction on transition Reynolds numbers. As expected, the impact was found to be stronger at higher inflow velocities, following from resulting deviations of the shape factor from increasing BL edge velocity and higher suction mass flow.

Due to the wall normal suction, transition shifts initially nearly linearly downstream at an increasing suction rate, until from a suction coefficient $c_Q = -0.00025$ only a small additional transition delay was observed. LST comparisons demonstrate, that all amplified modes in the nose region are completely damped by the suction panel from this c_Q limit. A slight additional shift at growing suction rates was assigned to the reduced displacement thickness behind the suction panel, which amplifies other frequencies in the thinner BL.

For a completely non-suction closed wall, the comparison of infrared visualization and stability calculation at large inflow velocities above $40 \frac{m}{s}$ yields critical N-factors of $N_{crit} \approx 10.5$. For $20 \frac{m}{s}$, the lower value of $N_{crit} \approx 9.6$ can also be attributed to the significantly delayed transition at this lower Reynolds number. The resulting widening of the transition region is visible in the corresponding infrared image and the N-factor diagram. According to the LST assumptions, the empirical N_{crit} is also influenced, since the linear approach strictly speaking loses its validity for this extended transitional stage.

As shown by former HLFC experiments on tail models, suction walls may significantly reduce critical N-factors in comparison with transition data from closed walls for TS as well as for crossflow instabilities. This effect is often related to roughness influences from the suction surface porosity, while the pressure gradient in the suction region may also cause a pressure difference between BL flow and the underlying chamber, which in turn locally causes blowing or at least reduced suction in low pressure regions. Another possible reason is expected by interactions of Tollmien Schlichting waves in the BL with unstable modes in the suction chamber flow. This could explain the observed reduction of N_{crit}. To clarify dominant influences, inflow velocities and suction rates will need higher resolution by additional flow conditions and mass flow rates, as planned in future NWB campaigns.

In addition, validation of TS mode predictions from LST was carried out by hot-wire measurements, which were used to calculate energy spectra of the boundary layers. By this way, properties of the critical TS waves were taken from spectral data in comparison with LST output. As a result, good agreement of measured and predicted relevant mode-frequencies was shown.

These experiments on a modular flat plate model with interchangeable suction panels in the DNW-NWB facility provide a good overview of the aerodynamic requirements with respect to laminar flow control by BL suction and allow new insights for different suction techniques. Particularly, even secondary effects could be observed with this setup, counteracting the primary effect of boundary layer stabilization by the modified velocity profile and thus decreasing the effectiveness of the suction wall by reducing N_{crit}. Different possible mechanisms were already identified as sources of

these reduced critical N-factors for porous walls, and further experiments with additional inflow conditions and suction rates are scheduled. Within this scope, also hot-wire measurements of the suction BL above the porous wall will be carried out to determine properties of the suction BL. To exploit the full potential of the modular plate configuration, variations of the area and position of different suction panels are intended.

Additional capabilities of this test rig for suction panels, like a free positioning of additional hot-wire traverses for velocity profiles and spectra or influences of heated surfaces, show the potential of this technique for global research on laminar flow control by boundary layer stabilization. Future experiments, exploiting the modularity of the model, are planned by manufacturing suction panels with different etched porous foils and welded metal fabric for structural stabilization below within the scope of the European Clean-Sky2-NACOR project.

References

1. Krishnan, K.S.G., Bertram, O., Seibel, O.: Review of hybrid laminar flow control systems. Progress Aerosp. Sci. **93**, 24–52 (2017)
2. Rohardt, C.-H., Seitz, A., et al.: Simplified-HLFC/ Entwurf eines Seitenleitwerks mit Hybrid-Laminarhaltung für den Airbus A320. In: German Society for Aeronautics and Astronautics (DGLR), 60. Deutscher Luft- und Raumfahrtkongress 27.-29. September, 2011 Bremen, Germany (2011), https://elib.dlr.de/74544/1/DGLR-Paper-27-29-9-2011-Bremen.pdf
3. Schrauf, G., Geyr, H.V.: Simplified hybrid laminar flow control for the A320 fin part 2: evaluation with the e^N-method. In: AIAA SciTech Forum 11-15 & 19-21 January 2021, Virtual Event, AIAA-2021-1305 (2021), https://doi.org/10.2514/6.2021-1305
4. Geyr, H.V.: Schlussbericht VER2SUS / Institut für Aerodynamik und Strömungstechnik, DLR Braunschweig. Technical Report, Airbus (2015)
5. Bergmann, A.: The aeroacoustic wind tunnel DNW-NWB. In: 18th AIAA/CEAS Aeroacoustics Conference (33rd AIAA Aeroacoustics Conference) 04 - 06 June 2012, Colorado Springs (2012), https://doi.org/10.2514/6.2012-2173

6. Horn, M., Seitz, A., Schneider, M.: Novel taylored skin single duct concept for HLFC fin application. In: 7th European Conference for Aeronautics and Space Sciences (EUCASS). Milan, Italy (2017), https://doi.org/10.13009/EUCASS2017-44, Corpus ID: 139423493

7. Schwamborn, D., Gerhold, T., Heinrich, R.: The DLR TAU-code: recent applications in research and industry. In: ECCOMAS CFD 2006 Conference, 2006-04-09 - 2006-08-09, The Netherlands (2006), https://elib.dlr.de/22421/

8. Schrauf, G.: COCO—a program to compute velocity and temperature profiles for local and nonlocal stability analysis of compressible. Conical Boundary Layers with Suction, ZARM Tecnical Report (1998)

9. Schrauf, G.: LILO 2.1 User's guide and tutorial, Bremen, Germany, GSSC Technical Report No. 6, modified Version 2.1 (2006)

10. Seitz, A.: Messkörper, Durchflussmesssystem und Computerprogramm dafür., Patent No. DE202014104037U1 (2014)

11. Breitenstein, C.: Auswertung experimenteller Untersuchungen einer ebenen Platte mit hybrider laminarer Strömungskontrolle, DLR-IB-AS-BS-2020-78, ISSN 1614-7790. DLR Technical report (2020)

12. Rohardt, C.H., Küpper, A.: Determination of the NTS-factor for the DNW-NWB. In: 19th DGLR-Fach-Symposium STAB, 4.-5. November 2014, Munic, Germany (2014), https://elib.dlr.de/95445/

13. Methel, J., Forte, M.: An experimental study on the effects of two-dimensional positive surface defects on the laminar-turbulent transition of a sucked boundary layer. Exp. Fluids **60**, 94 (2019). https://doi.org/10.1007/s00348-019-2741-2

14. Grappadelli, M.C., Scholz, P., et al.: experimental investigations of boundary layer transition on a flat-plate with suction. In: AIAA 2021-1452, AIAA Scitech Jan 1-4 2021, virtual event, https://doi.org/10.2514/6.2021-1452 (2021)

15. Mühlmann, P.: Softwaregestützte Transitionserkennung mit Hilfe von Infrarotaufnahmen im Flugversuch, DLR presentation (2019)

16. Schrauf, G.: On allowable step heights: lessons learned from the ATTAS and F100 flight tests. In: 7th European Conference on Computational Fluid Dynamics (ECFD 7), ECCOMAS, 11-15 June 2018, Glasgow, UK (2018), http://congress.cimne.com/eccm_ecfd2018/admin/files/filePaper/p409.pdf

17. Backhaus, K., Lüdeke, H.: Direct numerical simulation of TS-waves behind a generic step of a laminar profile in the DNW-NWB wind tunnel. In: Greener Aviation Conference. 11-13 October 2016, Brussels, Belgium (2016), https://elib.dlr.de/107689/1/GA2016_DNS_Luedeke.pdf

18. Nenni, J.P., Gluyas, G.L.: Aerodynamic design and analysis of an LFC surface. In: Astronautics & Aeronautics, Vol. 4, No. 7, pp. 52–57 (1966)

19. Iglisch, R.: Exakte Berechnung der laminaren Grenzschicht an der längsangeströmten ebenen Platte mit homogener Absaugung. Schriften der deutschen Akademie der Luftfahrtforschung (1944)

20. Tilton, N., Cortelezzi, L.: Stability of boundary layers over porous walls with suction. AIAA J. **53**(10), 2856–2868 (2015)